

Late Paleogene emergence of a North American loess plateau

Majie Fan, Ran Feng, John W. Geissman, Christopher Poulsen

Table DR1. GPS locations of the four studied sites

Site	Location	Latitude (°N)	Longitude (°W)	Elevation (m)
WS	Beaver Divide	42.611099	108.273924	1964
LTG	Flagstaff Rim	42.629369	106.765294	2015
EF	Douglas	42.610434	105.251476	1536
LG	Toadstool Geologic Park	42.851585	103.582744	1174

Note elevations were taken at the transitions from fluvial to eolian environments.

Table DR2. Lithofacies description and interpretation

Lithofacies	Description	Interpretation
Fluvial units		
Conglomerate	Underlies sandstone when presents, generally <1 m thick, clast-supported, massive or normal grading, poorly sorted, clasts are subangular-subrounded	Lag deposits
Sandstone	Medium- to coarse-grained, cross-stratified or horizontally stratified, 0.5-3 m thick, thick beds often have erosional bases and contain granules and pebbles at the bases, normal grading, poorly-moderately sorted, subangular-subrounded	Thick beds are cut and fill in waning stage of flows; thin beds are crevasse splay
Mudstone	Massive or laminated, typically contain pedogenic features such as mottling, root traces, and carbonate nodules, sometime contain floating granules	Pedogenically modified overbank

Aeolian units		
Siltstone and fine-grained sandstone	Massive, well sorted, well rounded	Aeolian deposits

Interpretation of fluvial facies is based on Miall (2014).

Details of Analytical Methods

Samples for grain-size analysis and rock magnetic property determinations were obtained from both eolian and fluvial lithofacies by trenching until fresh rock was exposed. Sedimentary rocks with mean grain size larger than medium sand are present in the fluvial lithofacies, but were not collected for grain-size analysis.

About 0.2 g of samples for grain size analysis were first gently powdered using ceramic mortar and pestle. Powders were loaded into 50 ml beakers with 10 ml of 10% H₂O₂. Samples were left on hot plate of 100 °C for ~10 m to ensure the complete removal of organic matter. Carbonate minerals were removed by gradual addition of 10 ml of 10% HCl, and digestion on hot plate for another 10 minutes. After cooling, samples were transferred to 15 ml centrifuge tubes and washed at last three times using DI water. Before analysis, 5 ml of 10% Na₄P₂O₇·10H₂O were added and the samples were dispersed in an ultrasonic bath for 3 minutes. Samples were then analyzed using a Malvern Master Sizer 2000, which has a size detection range of 0.02–2000 μm and analytical error of ~1%. Mean grain size, sorting, and distribution were used to display the differences between the two lithofacies (Figs. 2; 3). Five representative samples (three from the eolian lithofacies in the WS, LTG, and EF sections, and two from the fluvial lithofacies in the WS and EF sections) were examined using a JEOL JSM-IT100 USA scanning electron microscope (SEM)

(Department of Geoscience, University of Texas at Dallas) after the removal of carbonate minerals (Fig. 3; DR1).

Samples used for rock magnetic property determinations were disaggregated, but not crushed, and tightly packed into 7 cc standard IODP plastic boxes. Bulk magnetic susceptibility (MS) was measured on an AGICO KLY-3S Kappabridge. Anhyseretic remanent magnetization (ARM) was applied using an ASC Scientific D-2000 alternating field demagnetizer with a peak decaying alternating field of 100 mT in the presence of a direct current bias field of 0.1 mT. Isothermal remanent magnetization to saturation (SIRM) acquisition was applied in a progressively increasing field up to a maximum of 4 T. A field of 4 T allows high coercivity (i.e., hematite) specimens to reach full saturation. IRM acquisitions were applied in 30 steps using an ASC Scientific IM-10-30 impulse magnetizer. ARM and SIRM intensities were measured with either an AGICO JR5A or JR6A spinner magnetometer or a 2G Enterprises pulse-cooled superconducting rock magnetometer.

Stratigraphic Relationship between Transitions and Dated Volcanic Ashes

Although biotite and anorthoclase $^{40}\text{Ar}/^{39}\text{Ar}$ age data have been reported from several volcanic ashes in the White River Formation in the LTG, EF, and LG sections, a systematic comparison of recalculated $^{40}\text{Ar}/^{39}\text{Ar}$ ages, relative to Fish Canyon sanidine at 28.201 Ma, and zircon U-Pb dates of the same ashes in the LTG and LG sections suggest that the ash zircon U-Pb dates are more accurate (Sahy et al., 2015).

In the LGT section, the transition to eolian deposition is ~10 m stratigraphically

below ash F (Sahy et al., 2015). In the EF section, the transition is ~10 m stratigraphically below ash 7 and ~20 m stratigraphically above ash 5 (Evanoff, 1990). In the LG section, the transition is ~25 m stratigraphically below the Lower Whitney Ash (LWA), and ~30 m stratigraphically above Serendipity (SDP) ash (Sahy et al., 2015).

Details of Paleoclimate Simulation

Paleoclimate simulations were carried out using ECHAM5 at T106 horizontal resolution (~100 km grid space horizontally) with 19 vertical levels from ~1000 hPa to 10 hPa (Roeckner et al., 2003), with boundary conditions (land surface type, sea surface temperature, paleotopography and continental configuration) prescribed based on Eocene proxy reconstructions. All simulations were run with prescribed monthly sea surface temperature and reached equilibrium within 5 model years. Our model results (Fig. 4) represent the mean of the following 30 model years, which exhibits less than 0.01 °C/year trend of mean surface temperatures.

Boundary conditions

CO₂ level was prescribed to be 1120 ppm for the Eocene simulations (Beerling and Royer, 2011). Concentrations of other trace gases were prescribed to be pre-industrial. Eocene boundary conditions including global geography, topography, vegetation and SSTs are prescribed based on several studies (Sewall et al., 2000; Sewall and Sloan, 2006; Feng et al., 2013). In order to capture large-scale features of global cooling at the Eocene-Oligocene transition, we prescribed an eastern Antarctic ice sheet according to the combined proxy and model reconstruction (Deconto and Pollard, 2003), a 560 ppm drop in CO₂ level, and 5 °C annual sea surface temperature

(SST) cooling at both poles (Liu et al., 2009) by adding Gaussian weights to zonal mean SSTs: $-5 \times \cos\left(\frac{SST - SST_{min}}{SST_{max} - SST_{min}} \times \frac{\pi}{2}\right)$ (Fig. DR3).

Protracted crustal shortening and thickening associated with subduction of the Farallon plate beneath western North America resulted in a high Cordillera mountain belt in the western USA by the earliest Cenozoic (DeCelles, 2004). The hinterland was at least 2 km high during the Late Cretaceous (Snell et al., 2014), and experienced major extension and elevation drop during the Neogene (Wernicke et al., 1987), while the middle Eocene-Oligocene topography history remains controversial because of paucity of paleoelevation records (Constenius, 1996; Mix et al., 2011; Chamberlain et al., 2012; Cassel et al., 2014; Cassel et al., 2018). Spatial pattern of paleoelevation data suggests there was a southward trend of developing high topography (~3.5 km) from the northern to southern Cordillera hinterland during the middle Eocene-Oligocene (Mix et al., 2011; Chamberlain et al., 2012). However, geologic observations show extension in the hinterland as early as the middle Eocene (Wernicke et al., 1987; Constenius, 1996) and another paleoelevation study suggests that the southern Cordillera was ~2.5 km high during the latest Eocene (Cassel et al., 2014). In our simulations, we refine topography of the western USA to represent two end members of topographic scenarios proposed for this region during the late Eocene and early Oligocene (Fig. DR3).

The first scenario assumes that the high Cordilleran hinterland continued into the middle Eocene (Fig. DR3), and subsequent crustal extension and erosion lowered topography. Based on a paleoelevation study that suggests Nevada was at ~2.5 km during the latest Eocene (Cassel et al., 2014), and another study in the northern Basin

and Range that suggests local basin elevation was below 1.5 km during the Miocene (Lechler et al., 2013), we assume that the Cordillera hinterland dropped from ~3 km in the middle Eocene to ~2 km in the late Eocene.

The second scenario assumes that the Cordillera experienced rejuvenated surface uplift, and that the high-elevation area expanded southward during the middle Eocene-Oligocene in response to mantle lithosphere delamination associated with the removal of the Farallon slab (Mix et al., 2011; Chamberlain et al., 2012) (Fig. DR3). Paleoelevation reconstructions suggest that the mean elevation of the northern and central Cordillera was ~3.5 km during the middle Eocene, and the southern Cordillera was uplifted to ~3.5 km with an elevation gain of ~2 km during the latest Eocene and early Oligocene (Mix et al., 2011; Chamberlain et al., 2012). The Laramide ranges in the central Rockies were at least 2 km high while the intermontane basins remained low (<0.5 km) during the early Eocene (Fan et al., 2011), and regional uplift may have occurred during the late Eocene and was followed by mid- and late Cenozoic basin aggradation (Fan et al., 2014).

At the EOT, both scenarios would also concur with central Rockies basin aggradation, and shoreline regression induced by Antarctic glaciation (Fig. DR3e and h). Finally, sedimentary and stratigraphic evidence suggest that the foreland region of the Cordillera was occupied by several closed basins that contained large lakes during the early Eocene and some of the lakes lasted into the middle Eocene (e.g., Dickinson et al., 1988; Davis et al., 2009). Correspondingly, we prescribed a lake fraction of 50% for foreland basins in our middle Eocene simulations. The lake fraction is subsequently set to 0 for experiments featuring cooling at the EOT.

Model performances

ECHAM5 has shown reasonable skills in simulating many aspects of modern North American climate including the distribution of modern precipitation over western North America (Salathé, 2006; Cook et al., 2008) (Fig. DR4) and the strength and location of the Aleutian low and the storm track over the Pacific Northwest (Salathé, 2006). ECHAM5, coupled to the ocean model MPI-OM, simulates an Eocene climate with a lower equator-to-pole temperature gradient and ice-free Arctic at low $p\text{CO}_2$ of 560 ppmv (Heinemann et al., 2009), featuring high earth system sensitivity to greenhouse warming in the model, which is likely in line with proxy records (Caballero and Matthew, 2013).

Caveats of model results

Climate conditions across western North America during the early to middle Eocene are known to be difficult to simulate (Sloan, 1994; Sewall and Sloan, 2006). Paleoflora reconstructions suggest a warm and moist climate with annual temperatures between 10°C to 18°C and over 1 m annual precipitation at proxy sites across the Cordillera (Wilf et al., 1998). Yet, this warm and moist climate is not well simulated by many climate models (Huber and Caballero, 2011). Part of this mismatch can be explained by a steep meridional SST gradient simulated by models with tropics being too warm, mid- and high-latitude being too cold relative to proxy estimates. Different equator-to-pole SST gradient is shown to cause different meridional distribution of precipitation across the western North America (Feng et al., 2016). The difficulty of simulating a shallow meridional SST gradient is overcome with our prescribed SST approach. In our simulations, meridional SST gradient is

prescribed to be consistent with proxy estimates, and hence, minimizing the influence of model-proxy SST mismatches.

Nonetheless, the mismatch between model and terrestrial proxy data may also arise from the difficulty of aligning records to specific elevation. For example, Sewall and Sloan (2006) demonstrated that with a 1 km hinterland, simulated surface temperatures can achieve a good match with proxy records, yet precipitation is underestimated by model. Our current middle Eocene simulations with 1.5 km or 3 km hinterland elevation in the Southern Cordillera generally show moderate match with proxy precipitation (Fig. DR5a and b). Yet, with 3-km hinterland in the Southern Cordillera, simulated surface temperatures at the proxy sites are much cooler compared to the records (Fig. DR5a). This mismatch may disapprove a high elevation southern Cordillera during the middle Eocene, and hence supports our argument for the late Eocene uplift. Nonetheless, it is also possible that our model underestimates terrestrial temperature sensitivity to CO₂ forcing. It remains unclear what could be the cause for the latter (Lunt et al., 2012).

Calculation of surface moist enthalpy

Moist enthalpy (M_e) is defined as:

$$M_e = C_p' T + L_v q$$

C_p' is the specific heat capacity at constant pressure of moist air; T (K) is the surface temperature (K); L_v ($J\ kg^{-1}$) is the latent heat of evaporation for temperatures between 238 and 308 K (List, 1978); q is the specific humidity (kg/kg). Further, the specific heat capacity for moist air is calculated as:

$$C_p' = C_p(1-q) + C_w q$$

where C_w and C_p are the specific heat of liquid water ($4190 \text{ J kg}^{-1} \text{ K}^{-1}$) and dry air ($1004 \text{ J kg}^{-1} \text{ K}^{-1}$). For our simulations, we use 2 m air T and q to calculate the surface M_e . Following reversible moist adiabatic movements of an air parcel along a flat surface, M_e is conserved. This conservation property tracks air masses with unique thermodynamic characteristics. In our simulations, with uplifted Southern Cordillera, we detect a clear signal of tropical air mass (high in moist enthalpy) intrusion from Gulf of Mexico in the lee of the Cordillera corresponding to the anomalous southerlies from the Gulf (Fig. DR6) and weakening of westerlies in the windward side of the Cordillera from April to October, consistent with the theory arguing for generation of monsoonal circulation by the barrier effect of high mountains (Boos and Kuang, 2010) (Fig. DR6d to e). Opposite responses are simulated with elevation reduction of the Cordillera (Fig. DR6a and b).

Additional References

Beerling, D.J., and Royer D.L., 2011, Convergent Cenozoic CO_2 history: *Nature Geosciences*, v. 4, p. 418–420.

Boos, W.R., and Kuang, Z., 2010, Dominant control of the South Asian monsoon by orographic insulation versus plateau heating: *Nature*, v. 463, p. 218–222.

Caballero, R., and Matthew, H., 2013, State-dependent climate sensitivity in past warm climates and its implications for future climate projections: *Proceedings of the National Academy of Sciences of the United States of America*, v. 110, p. 14162–14167.

- Cassel, E.J., Breecker, D.O., Henry, C.D., Larson, T.E., and Stockli, D.F., 2014. Profile of a paleo-orogen: High topography across the present-day Basin and Range from 40 to 23 Ma: *Geology*, v. 42, p.1007–1010.
- Cassel, E.J., Smith, M.E., and Jicha, B.R., 2018, The Impact of Slab Rollback on Earth's Surface: Uplift and Extension in the Hinterland of the North American Cordillera: *Geophysical Research Letter*, v. 45, doi.org/10.1029/2018GL079887.
- Chase, C.G., Gregory-Wodzicki, K.M., Parrish-Jones, J.T., and DeCelles, P.G., 1998, Topographic history of the western Cordillera of North America and controls on climate, *in* Crowley T.J., and Burke, K., eds., *Topographic Evolution of the Western North American Cordillera: Tectonic Boundary Conditions for Climate Model Simulations*, New York, Oxford University Press, p. 73-99.
- Constenius, K.N., 1996, Late Paleogene extensional collapse of the Cordilleran foreland fold and thrust belt: *Geological Society of America Bulletin*, v. 108, p. 20–39.
- Cook, K.H., Edward, E.K., Launer, Z.S., and Patricola, C.M., 2008, Springtime intensification of the Great Plains low-level jet and Midwest precipitation in GCM simulations of the twenty-first century: *Journal of Climate*, v. 21, p. 6321–6340.
- Deconto, R.M., and Pollard, D.A., 2003, coupled climate–ice sheet modeling approach to the early Cenozoic history of the Antarctic ice sheet: *Palaeogeography, Palaeoclimatology, Palaeoecology*, v. 198, p. 39–52.
- Dickinson, W.R., Klute, M.A., Haynes, M.J., Janecke, S.U., Lundin, E.R., McKittrick, M.A., and Olivares, M.D., 1988, Paleogeographic and paleotectonic

- setting of Laramide sedimentary basins in the central Rocky Mountain region:
Geological Society of America Bulletin, v. 100, p.1023–1039.
- Fan, M., DeCelles, P.G., Gehrels, G.E., Dettman, D.L., Quade, J., and Peyton, S.L.,
2011, Sedimentology, detrital zircon geochronology, and stable isotope
geochemistry of the lower Eocene strata in the Wind River Basin, central
Wyoming: Geological Society of America Bulletin, v. 123, p. 979–996.
- Fan, M., Heller, P., Allen S.D., and Hough, B.G., 2014, Middle Cenozoic uplift and
concomitant drying in the central Rocky Mountains and adjacent Great Plains:
Geology, v. 42, p. 540–550.
- Feng, R., Poulsen, C.J., and Werner, M., 2016, Tropical circulation intensification
and tectonic extension recorded by Neogene terrestrial $\delta^{18}\text{O}$ records of the
western United States: Geology, v. 44, p. 971–974.
- Heinemann, M., Jungclauss, J. H., and Marotzke, J., 2009, Warm Paleocene/Eocene
climate as simulated in ECHAM5/MPI-OM: Climate of the Past, v. 5, p. 85–802.
- Huber, M., and Caballero, R., 2011, The early Eocene equable climate problem
revisited: Climate of the Past, v. 7, p. 603–633.
- Koch, P.L., Zachos, J.C., and Dettman D.L., 1995, Stable isotope stratigraphy and
paleoclimatology of the Paleogene Bighorn Basin (Wyoming, U.S.A.):
Palaeogeography, Palaeoclimatology, Palaeoecology, v. 115, p. 61–89.
- Lechler, A.R., Niemi, N.A., Hren, M.T., and Lohmann, K.C., 2013, Paleoelevation
estimates for the northern and central proto-Basin and Range from carbonate
clumped isotope thermometry: Tectonics, v. 32, p. 1–22.

- List, R., 1978, The Formation of Rain. Transactions of the Royal Society of Canada IV, V, XV, p. 333–347.
- Liu, Z., Pegani, M., Zinniker, D., DeConto, R., Huber, M., Brinkhuis, H., Shah, S.R., Leckie, R.M., and Pearson A., 2009, Global Cooling During the Eocene-Oligocene Climate Transition: Science, v. 323, p. 1187–1190.
- Lunt, D.J., Dunkley Jones, T., Heinemann, M., Huber, M., LeGrande, A., Winguth, A., Loptson, C., Marotzke, J., Roberts, C.D., Tindall, J., Valdes, P., and Winguth, C., 2012, A model–data comparison for a multi-model ensemble of early Eocene atmosphere–ocean simulations: EoMIP: Climate of the Past, v. 8, p. 1717–1736.
- Miall, A.D., 2014, Fluvial Depositional Systems. Springer-Verlag, Berlin, p.1–316.
- Salathé, E.P. Jr, 2006, Influences of a shift in North Pacific storm tracks on western North American precipitation under global warming: Geophysical Research Letters, v. 33, L19820.
- Sewall, J.O., and Sloan, L.C., 2006, Come a little bit closer: A high-resolution climate study of the early Paleogene Laramide foreland: Geology, v. 34, p. 81–84.
- Sewall, J.O., Sloan, L.C., Huber, M., and Wing, S., 2000, Climate sensitivity to changes in land surface characteristics: Global and Planetary Change, v. 26, p. 445–465.
- Sloan, L.C., 1994, Equable climates during the early Eocene: significance of regional paleogeography for North American climate: Geology, v. 22, p. 881–884.
- Snell, K.E., Koch, P.L., Druschke, P., Foreman, B.Z., and Eiler J.M., 2014, High elevation of the ‘Nevadaplano’ during the Late Cretaceous: Earth and Planet Science Letters, v. 386, p. 52–63.

Wilf, P., Wing, S.L., Greenwood, D.R., Greenwood, C.L., 1998, Using fossil leaves as paleoprecipitation indicators: An Eocene example: *Geology*, v. 26, p. 203–206.

Wing, S.L., and Greenwood, D.R., 1993, Fossils and fossil climate: The case for equable continental interiors in the Eocene: *Philosophical Transactions of the Royal Society of London, Series B, Biological Sciences*, v. 341, p. 243–252.

Figures

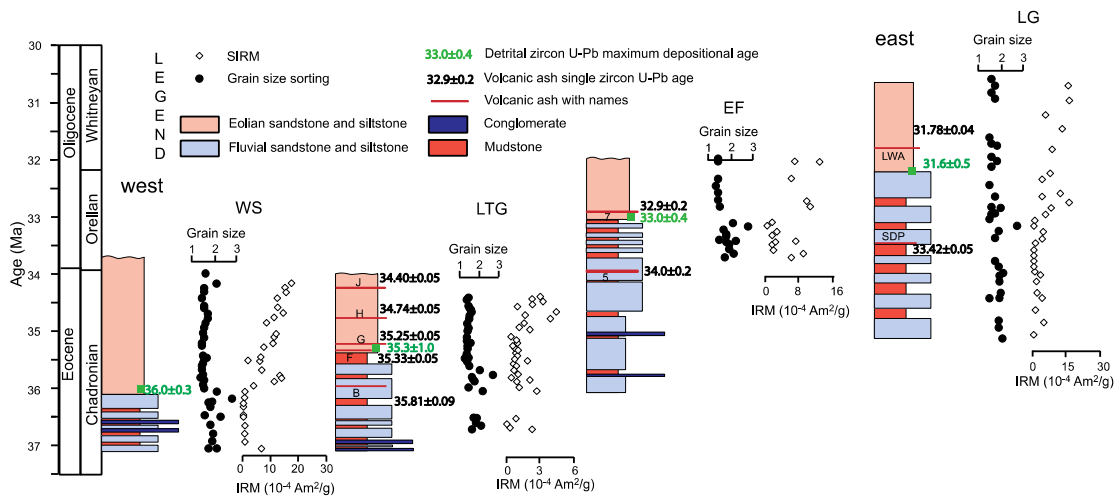


Figure DR1. Grain-size sorting and bulk SIRM intensity data collected from the WS, LTG, EF, LG sites are placed in a chronostratigraphic framework.

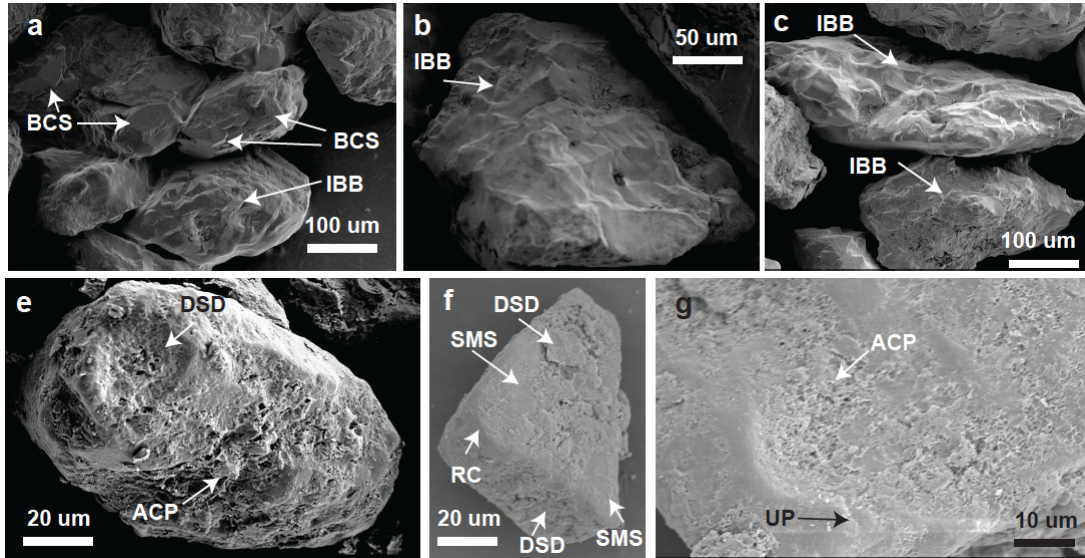


Figure DR2. SEM images of quartz grains in fluvial sandstones (a, b, c). Surface textures include broken cleavage surfaces (BCS) and irregular breakage blocks (IBB). Note angular to subangular edges. Images a and b are from the WS section, and c is from the EF section. SEM images of quartz grains in eolian sandstones and siltstones (e, f, g). Surface textures include adhering clay particles (ACP), dish-shaped depressions (DSD), upturned plate (UP) on the edges of grains, rounded corner (RC), and smooth precipitation surfaces (SMS). Note smoothness of surface. Images e is from the EF section, f is from the WS section, and g is from the LTG section.

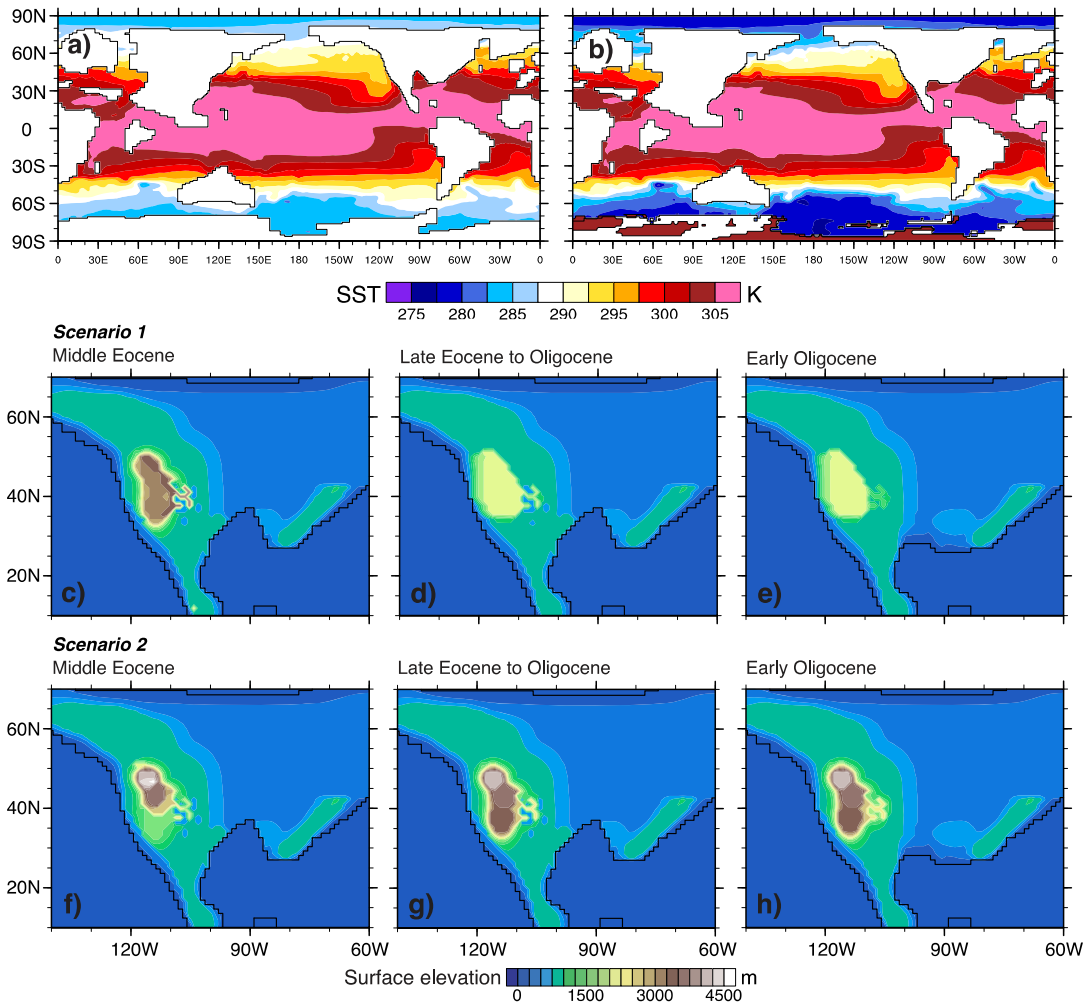


Figure DR3. Prescribed SSTs, land-sea mask, Antarctic ice sheet for cases featuring middle Eocene (a) and early Oligocene (b). Two topographic scenarios and shoreline locations of middle Eocene (c and f) and early Oligocene (d and e, g and h).

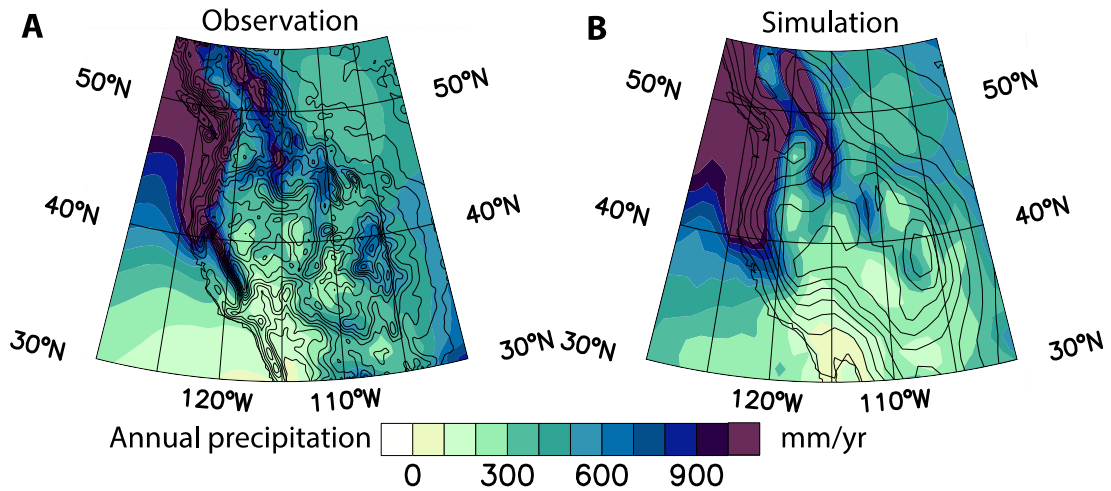


Figure DR4. Present-day observational (a) and ECHAM5 simulated precipitation (b) of the western USA. Present-day observation is from Modern-Era Retrospective Analysis for Research and Applications (MERRA) at 0.5° horizontal resolution (~ 50 km). Simulation data is from a prescribed SST simulation using present-day SSTs and 1° model resolution (the same resolution used in our paleo-runs). The observational data is smoothed using 9-point smoothing.

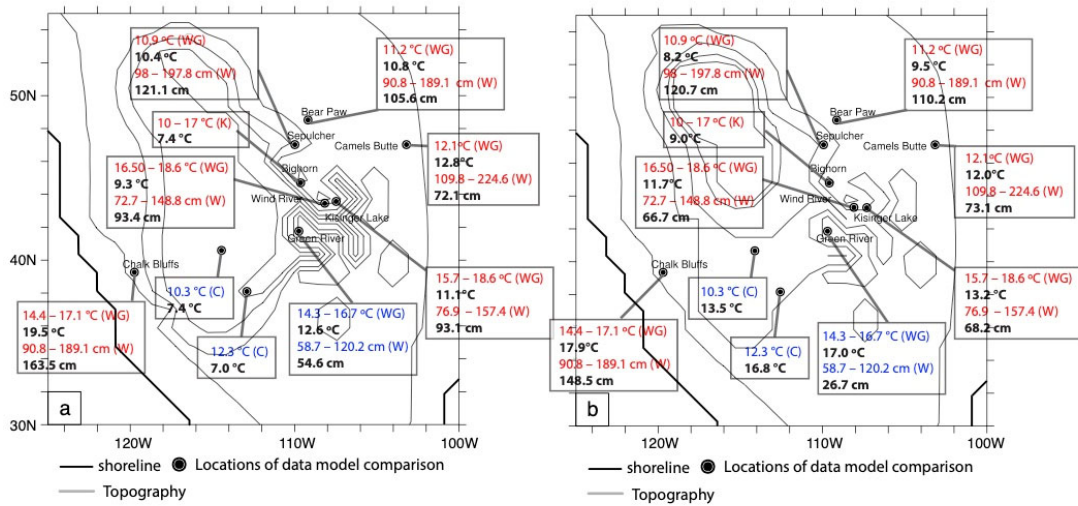


Figure DR5. Simulated (bold font) and proxy (regular font) precipitation and temperature estimated from early to middle Eocene (55 – 45 Ma, colored in red) and late middle Eocene (39 – 42 Ma, colored in blue) fossil flora of western North America (black dots). Proxy records are from references, including WG: Wing and Greenwood (1993), W: Wilf et al. (1998), C: Chase et al. (1998), and K: Koch et al. (1995). Coastal lines are shown in bold. Topographic contours are shown for 0.8, 1.5, 2.8, 3.3 and 3.7 km.

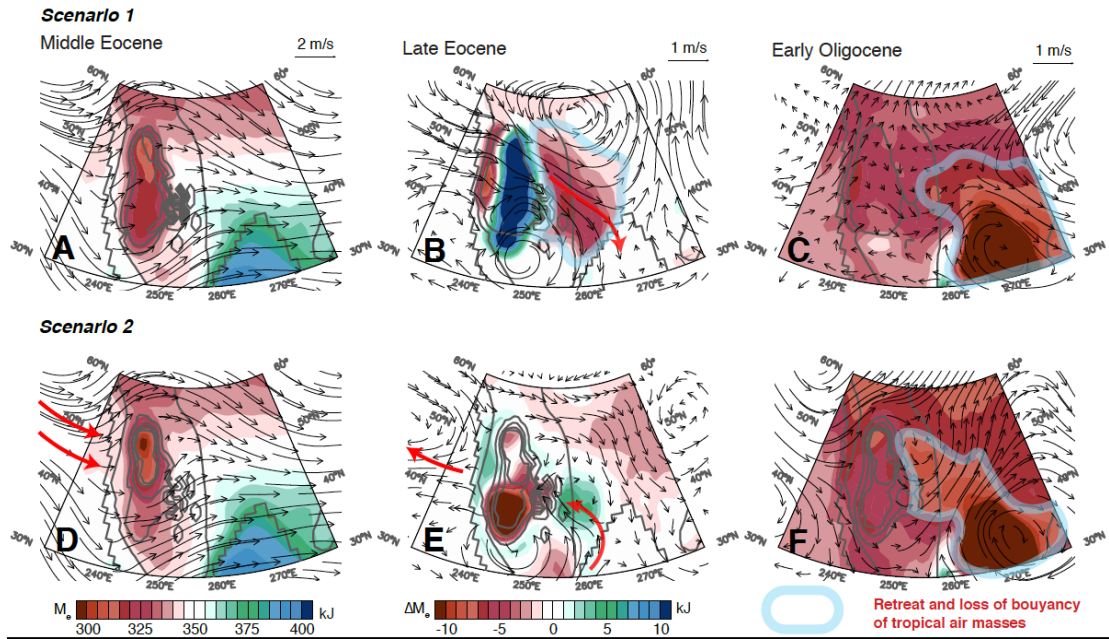


Figure DR6. Warm season (May to September) climatology (M_e and 700 hPa wind responses) (A and D) and changes in above surface moist enthalpy (ΔM_e) and 700 hPa wind responses (vectors) due to different topographic scenarios (B and E) and EOT climate cooling, shoreline regression, and basin fill (C and F). P-E responses are measured by subtracting simulation results featuring an earlier period from results featuring a later period. Think solid lines: topographic contour at elevations of 0.8, 1.5, 2.8, 3.3 and 3.7 km from the coast towards the Cordillera. Red arrows highlight climatology and key changes in the moisture transport path. Blue contours highlight regions with large reduction in M_e sourced from the Gulf of Mexico.

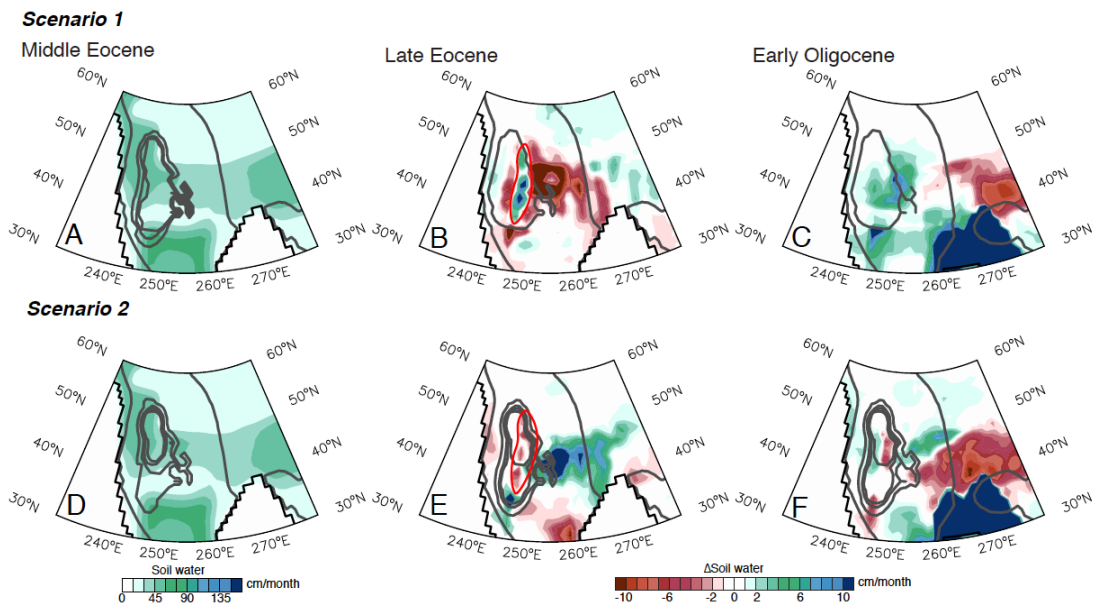


Figure DR7. Same as Figure DR6, but for annual mean soil water content (cm/month). Red contours in B and E highlight the contrasting changes in soil water content between two topographic scenarios. Think solid lines: topographic contour at elevations of 0.5, 1.5, 2.5, 3.0 and 3.5 km from the coast towards the Cordillera.

Data for grain size and rock magnetic properties

2020075_Dataset.xlsx